

# UC San Diego

## UC San Diego Previously Published Works

### Title

Metallofluorocarbon Nanoemulsion for Inflammatory Macrophage Detection via PET and MRI

### Permalink

<https://escholarship.org/uc/item/3gj2h5rk>

### Journal

Journal of Nuclear Medicine, 62(8)

### ISSN

0161-5505

### Authors

Wang, Chao  
Leach, Benjamin I  
Lister, Deanne  
et al.

### Publication Date

2021-08-01

### DOI

10.2967/jnumed.120.255273

Peer reviewed

---

---

# Metallofluorocarbon Nanoemulsion for Inflammatory Macrophage Detection via PET and MRI

Chao Wang<sup>1</sup>, Benjamin I. Leach<sup>1</sup>, Deanne Lister<sup>1</sup>, Stephen R. Adams<sup>2</sup>, Hongyan Xu<sup>1</sup>, Carl Hoh<sup>1</sup>, Patrick McConville<sup>1,3</sup>, Jing Zhang<sup>4</sup>, Karen Messer<sup>4</sup>, and Eric T. Ahrens<sup>1</sup>

<sup>1</sup>Department of Radiology, University of California San Diego, La Jolla, California; <sup>2</sup>Department of Pharmacology, University of California San Diego, La Jolla, California; <sup>3</sup>Invivo, Inc., Boston, Massachusetts; and <sup>4</sup>Moore's Cancer Center, University of California San Diego, La Jolla, California

---

Inflammation is associated with a range of serious human conditions, including autoimmune and cardiovascular diseases and cancer. The ability to image active inflammatory processes greatly enhances our ability to diagnose and treat these diseases at an early stage. We describe molecular compositions enabling sensitive and precise imaging of inflammatory hotspots in vivo. **Methods:** A functionalized nanoemulsion with a fluorocarbon-encapsulated radiometal chelate (FERM) was developed to serve as a platform for multimodal imaging probe development. The <sup>19</sup>F-containing FERM nanoemulsion encapsulates <sup>89</sup>Zr in the fluororous oil via a fluorinated hydroxamic acid chelate. Simple mixing of the radiometal with the preformed aqueous nanoemulsion before use yields FERM, a stable in vivo cell tracer, enabling whole-body <sup>89</sup>Zr PET and <sup>19</sup>F MRI after a single intravenous injection. **Results:** The FERM nanoemulsion was intrinsically taken up by phagocytic immune cells, particularly macrophages, with high specificity. FERM stability was demonstrated by a high correlation between the <sup>19</sup>F and <sup>89</sup>Zr content in the blood (correlation coefficient > 0.99). Image sensitivity at a low dose (37 kBq) was observed in a rodent model of acute infection. The versatility of FERM was further demonstrated in models of inflammatory bowel disease and 4T1 tumor. **Conclusion:** Multimodal detection using FERM yields robust whole-body lesion detection and leverages the strengths of combined PET and <sup>19</sup>F MRI. The FERM nanoemulsion has scalable production and is potentially useful for precise diagnosis, stratification, and treatment monitoring of inflammatory diseases.

**Key Words:** fluorocarbon nanoemulsion; PET; MRI; <sup>19</sup>F; inflammation

**J Nucl Med 2021; 62:1146–1153**  
DOI: 10.2967/jnumed.120.255273

---

**I**nflammation is a defensive innate immune response toward invasive stimuli and features activation and recruitment of immune cells. Although beneficially promoting pathogen clearance and tissue recovery, uncontrolled inflammatory responses drive disease pathobiology. Conventional tissue contrast-based imaging methods, including proton MRI and CT, can detect non-cell-specific inflammation lesions at a late stage; however, molecular imaging methods

offer the potential for increased specificity, earlier diagnosis, and improved therapeutic outcomes. Thus, there is keen interest in developing molecular imaging probes with precise targeting to inflammatory cells and markers (1).

The PET probe <sup>18</sup>F-FDG serves as an imaging biomarker for numerous inflammatory diseases but can also have prominent uptake in tissues such as heart, kidney, and gastrointestinal tract, potentially confounding image interpretation for diseases affecting these regions (2,3). In the case of solid tumors and metastasis, it is challenging to distinguish between tumor-associated macrophages and tumor cells on <sup>18</sup>F-FDG PET scans, as both are metabolically active and take up the agent. Other small-molecule radiotracers targeting inflammatory markers, such as cytokines, translocator proteins, enzymes, and integrin receptors, have been designed for enhanced specificity and have shown varying degrees of success (4,5). Nanoparticle PET tracers for macrophages have also been explored, including <sup>18</sup>F- and <sup>64</sup>Cu-polyglucose (6,7) and <sup>89</sup>Zr-dextran (8).

The size and morphology of nanoemulsion droplets make them susceptible to endocytosis by phagocytic immune cells, providing a powerful cell-delivery approach for efficient intracellular macrophage labeling in situ. Intravenously administered fluorocarbon nanoemulsions enable background-free hotspot <sup>19</sup>F MRI detection (9). The nanoemulsion droplets are scavenged in situ by cells of the reticuloendothelial system (RES), particularly monocytes and macrophages but also neutrophils and dendritic cells (10). The fluororous droplets coalesce into phagocyte lysosomal vesicles and macropinosomes (11), thus escaping osmotic pressure-based cell efflux (12), and yield durable labeling, in contrast to small-molecule tracers (13). Fluorocarbons have a proven safety profile and a well-characterized biodistribution and pharmacokinetics. The biologic inertness and gas-dissolving property of fluorocarbons have made them major candidates for oxygen-carrying blood substitutes (14) since the 1980s. Moreover, clinical immunotherapeutic cells, prelabeled with a fluorocarbon nanoemulsion, have been longitudinally imaged with <sup>19</sup>F MRI after inoculation into cancer patients (15).

In this work, we investigated novel compounds for sensitive and precise inflammation imaging using PET and <sup>19</sup>F MRI. We synthesized a functionalized nanoemulsion (~160 nm in droplet size) to incorporate a fluorocarbon-encapsulated radiometal chelate (FERM) that captures <sup>89</sup>Zr into the fluororous phase of the preformed nanoemulsion via a simple premix step (Fig. 1A). <sup>89</sup>Zr has a relatively long half-life (3.3 d) matching the organ-retention time of many fluorocarbons used in biomedicine (e.g., perfluorooctylbromide, with a half-life of 5.1 d) (16) and is widely used in clinical

---

Received Aug. 12, 2020; revision accepted Nov. 12, 2020.  
For correspondence or reprints contact: Eric T. Ahrens, University of California San Diego, 9500 Gilman Dr., #0695, La Jolla, CA 92093.  
E-mail: eta@ucsd.edu  
Published online December 4, 2020.  
COPYRIGHT © 2021 by the Society of Nuclear Medicine and Molecular Imaging.

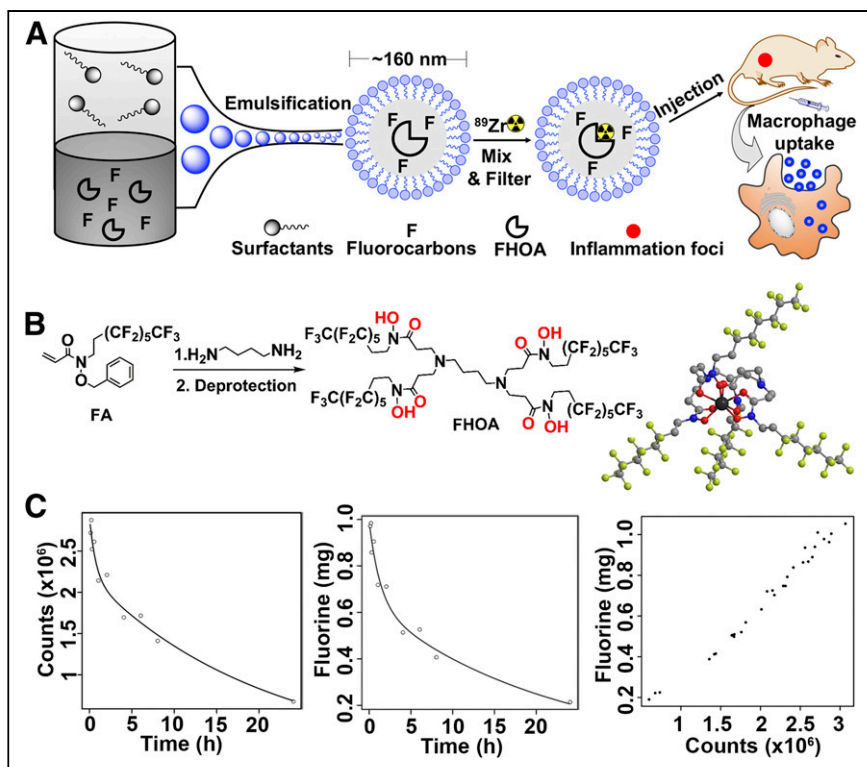


**FIGURE 1.** Preparation and pharmacokinetic analysis of FERM nanoemulsion. (A) Experimental workflow. (B) Chemical structure of FHOA and its simulated complex with  $Zr^{4+}$ . Black = zirconium; red = oxygen; blue = nitrogen; gray = carbon; yellow = fluorine; H omitted. (C) Pharmacokinetic analysis of FERM nanoemulsion (PFCE) in mouse as measured by decay-corrected  $\gamma$ -counts and fluorine content in blood samples (100  $\mu$ L, 3 mice per time point) drawn over 24 h. Biexponential fits are used to calculate decay half-lives. Scatterplot correlates  $\gamma$ -counts and fluorine content (Pearson  $r = 0.9933$ ). FA = fluorinated acrylamide.

trials to label monoclonal antibodies for PET (17). The highly hydrophobic nature of fluorocarbons helps exclude competition from water, cations, lipids, and proteins, which may contribute to the dissociation of  $^{89}Zr$  from the carrier. Nanoemulsions formulated with a chelate have a long shelf-life, and radiolabeling before use minimizes radiation-intensive steps for potential clinical trial use.

Using FERM, we demonstrated effective detection of macrophage-associated inflammation using multimodal PET and  $^{19}F$  MRI in murine models of acute infection, inflammatory bowel disease (IBD), and breast cancer. The results displayed robust whole-body lesion detection that leverages the strengths of PET (sensitivity),  $^{19}F$  MRI (low background), and  $^1H$  MRI and CT (high-resolution anatomic localization). Overall, the FERM nanoemulsion offers simplicity and highly specific targeting of phagocytic immune cells in vivo.

## MATERIALS AND METHODS

Details on the synthesis of fluorinated hydroxamic acid (FHOA) and the radiolabeled FERM nanoemulsion are provided in the supplemental materials (available at <http://jnm.snmjournals.org>). All animal experiments followed protocols that were approved by the University of California San Diego's Institutional Animal Care and Use Committee.

### Blood Circulation Time and Agent Stability In Vivo

The blood half-life of the FERM nanoemulsion (perfluoro-15-crown-5-ether, PFCE) was monitored using  $\gamma$ -counting and  $^{19}F$  nuclear MR (NMR). The  $^{89}Zr$ -labeled FERM was injected into C57BL6 mice ( $n =$

6,  $\sim 40$  g; Jackson Laboratory) via the tail vein at a dose of 3.145 MBq (0.2 mL). The mice were anesthetized using 1%–2% isoflurane in oxygen, and blood samples were collected from the retroorbital sinus using capillary pipettes. A 100- $\mu$ L blood sample was pipetted into a 5-mm NMR tube, followed by the addition of lysis buffer (100  $\mu$ L). The radioactivity of each sample was assayed and decay-corrected. After a 5-wk  $^{89}Zr$  decay, a sodium trifluoroacetate reference (25 mM) in  $D_2O$  (50  $\mu$ L) was added to the blood samples.  $^{19}F$  NMR spectra were acquired to calculate the fluorine content in the blood samples. A biexponential decay model was used to calculate blood half-lives.

### Carrageenan Acute Inflammation Model

$\lambda$ -carrageenan plant mucopolysaccharide (Sigma-Aldrich) was injected (2% in saline, 50  $\mu$ L) into the right paw of female CD1 mice (Envigo). Swelling of the paw was confirmed visually and by paw width caliper measurements. The FERM nanoemulsion was injected (3,700–37 kBq, 0.2 mL) through the tail vein, and  $^{19}F/^1H$  MRI, PET, and CT images were acquired 24 h after injection in isoflurane-anesthetized mice.

### IBD Model

IBD was induced in female C57BL/6 mice ( $n = 9$ ) by administration of 3% dextran sulfate sodium salt in drinking water ad libitum for 7 d before nanoemulsion injection. Control mice ( $n = 3$ ) received normal water. Disease progression was monitored daily by

body weight loss, stool score, and hemocult score (Supplemental Fig. 1). The  $^{89}Zr$ -labeled FERM nanoemulsion (3.7 MBq, 0.2 mL) was injected through the tail vein, and  $^{19}F/^1H$  MRI, PET, and CT images were acquired 24 h after injection.

### 4T1 Tumor Model

Luciferase-expressing 4T1-luc2 cells (CRL-2539-luc2; ATCC) were maintained in RPMI medium containing 10% fetal bovine serum and blasticidin, 8  $\mu$ g/mL. Cells ( $5 \times 10^6$ ) were suspended in 50  $\mu$ L of phosphate-buffered saline containing 50% Matrigel (Corning) and inoculated into the fourth mammary fat pad of female BALB/c mice (Envigo).

Tumor volumes were measured by calipers, and the mice were sorted into 2 groups ( $n = 5$  each) when the tumors reached a volume of 200–350  $mm^3$  (2-wk cohort) or 900–1,200  $mm^3$  (5-wk cohort). The  $^{89}Zr$ -labeled FERM nanoemulsion was injected into the mice via the tail vein at a dose of 3.7 MBq (200  $\mu$ L), and  $^{19}F/^1H$  MRI, PET, CT and bioluminescence images were acquired 24 h after injection.

### PET/CT Imaging

PET/CT data were acquired using Inveon (Siemens) and G8 (SOFIE) scanners. The animals were anesthetized using 1%–2% isoflurane in oxygen and warmed using heated pads to maintain body temperature throughout the procedure. PET data were acquired for 10 min at approximately 24 h after  $^{89}Zr$ -FERM injection.

### MRI

MRI was performed using a Bruker BioSpec 11.7-T system running ParaVision 6 software and a dual-tuned  $^{19}F/^1H$  38-mm volume coil

(Bruker BioSpin). The mice were anesthetized using 1%–2% isoflurane in oxygen, and body temperature was maintained throughout the procedure using heated air.  $^{19}\text{F}$  images were acquired using a RARE (rapid acquisition with relaxation enhancement) sequence (repetition time, 1 s; echo time, 20 ms; RARE factor, 8; field of view,  $30 \times 45$  mm; matrix size,  $32 \times 48$ ; coronal slice thickness, 2 mm [12 slices]; number of averages, 150; scanning time, 15 min). Anatomic  $^1\text{H}$  scans were also acquired using a RARE sequence (repetition time, 2 s; echo time, 20.5 ms; RARE factor, 8; number of averages, 10; scanning time, 1 min; slice thickness, 1 mm [24 slices]; field of view and orientation identical to those used to acquire the  $^{19}\text{F}$  images).

### Image Quantification and Visualization

Images were quantified using VivoQuant software (Invivo). PET data were calibrated using a phantom containing  $^{89}\text{Zr}$ . Footpad signals were quantified by placing a cylindrical region of interest (ROI) over the paws and integrating the signals. For analysis of IBD models, bone and bone marrow signals were segmented by thresholding CT images. Coarse ROIs were placed over the liver and spleen and segmented by thresholding the PET signal from  $3.7 \times 10^{-7}$  to  $7.4 \times 10^{-6}$  kBq. A single ROI was then placed over the peritoneum for subsequent analysis.  $^{19}\text{F}$  data were quantified from a phantom placed in the field of view. For each image, 3 ROIs were placed in the phantom and 3 in the background to determine signal values and errors. Histograms were produced using VivoQuant software, with ranges set from 0 to  $1 \times 10^{-4}$  percentage injected dose (%ID) per voxel for PET imaging and from 0 to  $3 \times 10^{24}$  fluorine atoms/mL for  $^{19}\text{F}$  MRI. For clarity, beds and phantoms were masked by thresholding the CT image to generate an ROI around the mouse and then exporting as a separate image. For display purposes, PET and  $^{19}\text{F}$  MRI were coregistered by applying a transformation derived from coregistration of CT and  $^1\text{H}$  images using an affine or non-linear transformation algorithm in VivoQuant, and images were rendered in pseudocolor.

### Statistics

The 2-sample unpaired *t*-test was used for significance analysis. A *P* value of less than 0.05 was considered significant. The statistical software R (<http://www.r-project.org>) was used for pharmacokinetic analysis of blood samples. The function “biexp” was used to build the biexponential model for estimation of 2-phase half-lives for both  $\gamma$ -counting and  $^{19}\text{F}$  NMR, and bootstrapping techniques were used to calculate 95% CIs.

## RESULTS

### Preparation and Characterization of FERM Nanoemulsion

To formulate the FERM nanoemulsion, we synthesized FHOA for  $\text{Zr}^{4+}$  binding. FHOA was prepared at gram scale using an azo-Michael reaction (18) between a fluoros acrylamide and primary diamine (Fig. 1B). FHOA shares the hydroxamic acid units of the hexadentate desferrioxamine, a commonly used  $\text{Zr}^{4+}$  chelator for immuno-PET (19). The FHOA chelate provides 8 oxygen coordination sites to saturate the  $\text{Zr}^{4+}$  sphere to avoid labile binding with  $\text{H}_2\text{O}$  and biomolecules, which are speculated to be a source of zirconium-desferrioxamine instability (20). Force-field simulation (Molecular Mechanics 2, ChemDraw; PerkinElmer) has shown the formation of a distorted square antiprismatic complex, with an averaged zirconium-oxygen length of 2.1 Å, close to the 2.2 Å calculated from the x-ray structure of zirconium-tetrahydroxamate (21). FHOA has a fluorine content of 54.26% and is soluble in perfluorooctylbromide up to 15 mM (at room temperature) and PFCE up to 2 mM with mild heating; both of these fluorocarbons have been used for  $^{19}\text{F}$  MRI (9,22). Titration of  $\text{ZrCl}_4$  (nonradioactive) into FHOA in solution caused attenuation and shifting of FHOA peaks

in  $^1\text{H}$  and  $^{19}\text{F}$  NMR (Supplemental Fig. 2); no peak change was observed beyond 1 equivalent, suggesting a 1:1 ratio for zirconium-FHOA binding. Binding of FHOA to  $\text{ZrCl}_4$  (1 equivalent) in solution was rapid, with completion in less than 20 min (Supplemental Fig. 3).

Among various biologically relevant metals,  $\text{Fe}^{3+}$  is the strongest competitor for  $\text{Zr}^{4+}$  chelate. Addition of  $\text{Fe}^{3+}$  to FHOA in nanoemulsion caused an increase in ultraviolet-visible light absorption at approximately 450 nm, which was then reduced by addition of  $\text{Zr}^{4+}$ , suggesting  $\text{Fe}^{3+}$  displacement by  $\text{Zr}^{4+}$  (Supplemental Fig. 2). Extinction of absorption at 450 nm was monitored and fitted, yielding biexponential decay half-lives of  $0.32 \pm 0.07$  h and  $2.91 \pm 0.26$  h. To further assess  $\text{Fe}^{3+}$  competition, we measured the change in the  $^{19}\text{F}$   $T_1$  relaxation time in the nanoemulsion on metal binding. Addition of  $\text{Fe}^{3+}$  to FHOA in nanoemulsion caused a 53% drop in  $T_1$  (from 1.2 to 0.6 s) due to the paramagnetic relaxation enhancement mechanism (23). Subsequent addition of  $\text{ZrCl}_4$  recovered the  $T_1$  to 0.96 s via displacement of strongly paramagnetic  $\text{Fe}^{3+}$  with  $\text{Zr}^{4+}$ . Conversely, addition of excess  $\text{Fe}^{3+}$  to zirconium-saturated nanoemulsion only decreased the  $T_1$  by 5.7%. These data indicate that  $\text{Zr}^{4+}$  forms a more stable complex with FHOA than does  $\text{Fe}^{3+}$ .

The FHOA was fully dissolved in the fluorocarbons before being formulated into the aqueous FERM nanoemulsion, as described in the supplemental materials, yielding a mean diameter of about 160 nm and a polydispersity index of less than 0.1 (Supplemental Table 1). Inclusion of FHOA (1 or 10 mM) had no statistically significant impact ( $P > 0.05$ ) on the nanoemulsion size or stability over at least 2 mo. Cells labeled with the FERM nanoemulsion showed no significant cytotoxicity over 48 h (Supplemental Fig. 4).

### Radiolabeling of FERM Nanoemulsion

Preformed perfluorooctylbromide or PFCE nanoemulsion (1 mL) containing chelate, and formulated with lipid-based surfactants, was radiolabeled by mixing with  $^{89}\text{ZrCl}_4$  (in 1 M HCl) at room temperature for 3 h. Unbound  $^{89}\text{Zr}$  was removed by a single gel-filtration step, resulting in a radiochemical yield of  $63.2\% \pm 6.5\%$  in an 0.8-mL elution. We also tested nanoemulsion radiolabeling using  $^{89}\text{Zr}$ -oxalate (in 1 M oxalic acid), for which, unlike  $^{89}\text{ZrCl}_4$ , neutralization was necessary to achieve efficient labeling. The radiolabeling yield of FERM was  $50.9\% \pm 4.7\%$  (pH 6.5) with  $^{89}\text{Zr}$ -oxalate 3 h after labeling. As a substitute for lipid surfactant, efficient radiolabeling of the nanoemulsion was also achieved with a triblock copolymer surfactant, Pluronic F68 (BASF), with a  $^{89}\text{ZrCl}_4$  yield of  $58\% \pm 7.1\%$  for FERM. We collected only a 0.8-mL elution to minimize unbound  $^{89}\text{Zr}^{4+}$  impurity and dilution of fluorine concentration (which is undesirable for  $^{19}\text{F}$  MRI). Overall, FERM nanoemulsion radiolabeling is flexible with respect to surfactant type, as it relies on an encapsulated chelate in the inert fluorocarbon core.

### In Vivo FERM Nanoemulsion Blood Stability and Half-Life

Nanoemulsion circulation half-life and in vivo stability were investigated in wild-type mice. The animals received a single intravenous injection of FERM nanoemulsion ( $n = 6$ , PFCE, 3.14 MBq,  $\sim 6 \times 10^{20}$  fluorine atoms) via the tail vein. Longitudinal blood samples over 24 h were assayed using both  $\gamma$ -dosimetry and  $^{19}\text{F}$  NMR (Fig. 1C). The  $\gamma$ -count data were decay-corrected, and the total fluorine content in the samples was determined by quantitative  $^{19}\text{F}$  NMR spectroscopy. We observed a strong correlation between the 2 methods (Pearson coefficient, 0.99), indicating retention of  $^{89}\text{Zr}$  in the  $^{19}\text{F}$ -containing nanoemulsion. The results demonstrated stability

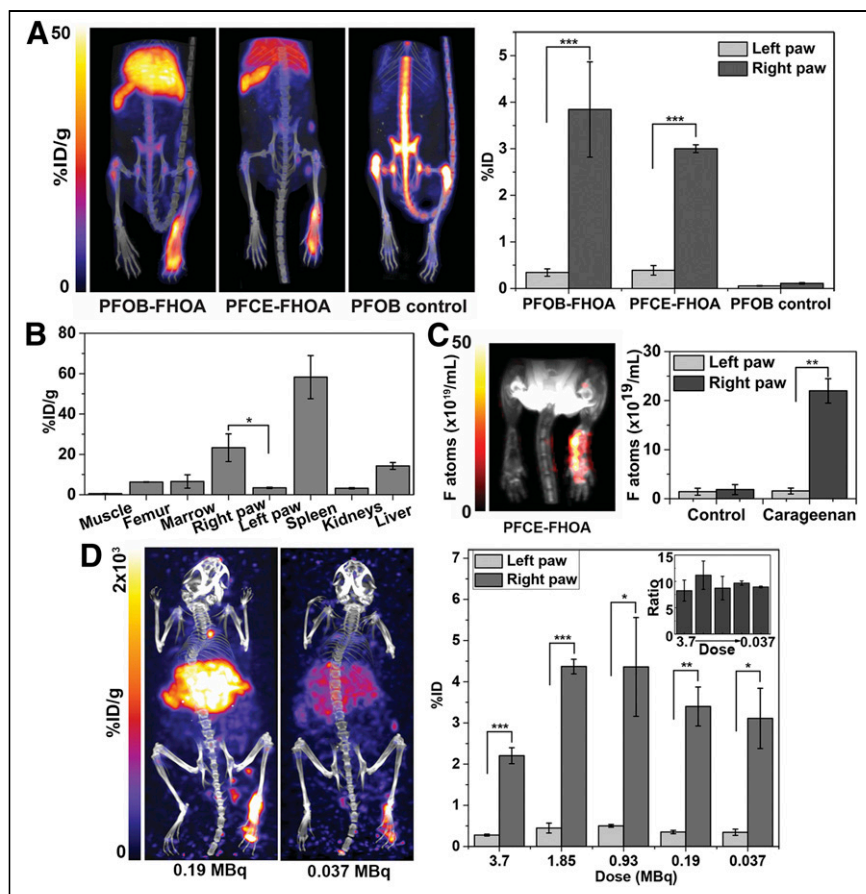


**FIGURE 2.** Visualization of acute footpad inflammation via in situ labeling of phagocytic immune cells with  $^{89}\text{Zr}$ -labeled FERM nanoemulsion. (A) Representative PET/CT images of mice 24 h after intravenous injection of FERM nanoemulsion or control nanoemulsion without FHOA (left), and ROI results for PET signal in paws (right). (B) Biodistribution of FERM nanoemulsion in excised tissues measured by  $\gamma$ -counting after imaging. (C) Composite  $^{19}\text{F}/^1\text{H}$  MRI (left) from mouse in A and quantification of fluorine content in footpads with and without carrageenan treatment. (D) Representative PET/CT images of mice injected with low doses of FERM nanoemulsion (left), and ROI results for PET signals in paws (right); inset shows signal ratio for right to left paws. Data are mean  $\pm$  SEM ( $n = 3$ ). \* $P < 0.05$ , unpaired  $t$  test. \*\* $P < 0.005$ , unpaired  $t$  test. \*\*\* $P < 0.001$ , unpaired  $t$  test.

of the complex in vivo for more than 24 h. The time-course data (Fig. 1C) displayed multiexponential behavior, and a 2-compartment biexponential model was used to estimate the half-lives. Bootstrapping techniques (24) were used to calculate the median and differences in half-lives at the 95% CI. For dosimetry, the analysis yielded median half-lives of 0.6 h (interquartile range, 0.2 h) and 14.5 h (interquartile range, 0.07 h), respectively. The  $^{19}\text{F}$  NMR method resulted in median half-lives of 0.90 h (interquartile range, 0.01 h) and 14.6 h (interquartile range, 0.11 h), respectively. We attribute the fast phase to perfusion and dilution of the agent in the bloodstream, and the slow phase to clearance of the agent from the blood by the RES, including uptake by monocytes and macrophages (25). The fast half-life was 11%–78% higher as measured by  $^{19}\text{F}$  NMR than as measured by the dosimetry method. The difference in the slow-phase decay between the 2 methods was less than 1%, which is insignificant.

#### Visualization of Acute Inflammation In Vivo

The FERM nanoemulsion is a versatile preclinical inflammation agent for a wide range of diseases. We initially investigated the

feasibility of PET and  $^{19}\text{F}$  MRI inflammation detection in an acute inflammation rodent model. The model uses an injection of  $\lambda$ -carrageenan plant mucopolysaccharide into the footpad of mice and is commonly used to test antiinflammatory drugs and immune response (26). The  $^{89}\text{Zr}$ -labeled FERM nanoemulsion was injected ( $n = 3$ , 3.7 MBq,  $\sim 6 \times 1,020$  fluorine atoms) by the tail vein 1 h after carrageenan treatment. PET/CT images were acquired 24 h thereafter to permit FERM uptake by the RES, including macrophages. On PET, mice receiving FERM, formulated with either perfluorooctylbromide or PFCE, displayed hotspots in the inflamed right paw, with little observable signal on the contralateral side (Fig. 2A). Prominent signals were also observed in the spleen and liver. Immunohistochemical results in the hind paws showed macrophage fluorocarbon uptake in situ after intravenous infusion (Supplemental Fig. 5), consistent with prior studies on various inflammation models (9,27). Control animals received either free  $^{89}\text{ZrCl}_4$  or  $^{89}\text{Zr}$ -treated nanoemulsion without chelate, and both displayed similar trafficking patterns (Fig. 2A; Supplemental Fig. 6); free  $^{89}\text{Zr}$  is taken up by bone (28).

We performed ROI analysis of the footpad PET signals. In FERM-injected animals (perfluorooctylbromide, 3.7 MBq), uptake in the right (inflamed) hind paw was  $3.8 \pm 1.0$  %ID, compared with  $0.34 \pm 0.08$  %ID in the left (control) hind paw. The mice were euthanized, and  $\gamma$ -counting of the excised hind paws confirmed differential uptake (Fig. 2B), with the right paw showing approximately 7-fold higher uptake than the left ( $23.3 \pm 11.9$  %ID/g vs.  $3.4 \pm 0.56$  %ID/g, respectively;  $n = 3$ ).

The bulk of the nanoemulsion was detected by dosimetry in the liver ( $14.2 \pm 2.9$  %ID/g) and spleen ( $58.2 \pm 2.9$  %ID/g). In animals injected with lipid-associated  $^{89}\text{Zr}$  perfluorooctylbromide nanoemulsion without chelate (3.7 MBq,  $n = 3$ ), uptake was  $0.11 \pm 0.01$  %ID/g and  $0.05 \pm 0.01$  %ID/g in the right and left paws, respectively. For the lipid-associated  $^{89}\text{Zr}$  perfluorooctylbromide nanoemulsion, the bulk of the activity was found in the bone. Activity was minimally detected in the liver and spleen, as was seen for free  $^{89}\text{Zr}$  (Supplemental Fig. 6).

A single dose of FERM nanoemulsion enabled multimodal  $^{19}\text{F}$  MRI and PET detection in the same subject. In the acute inflammation model, in vivo spin-density-weighted  $^{19}\text{F}$  and T2-weighted  $^1\text{H}$  multislice images were acquired, followed by PET/CT scans in the same mice. Both  $^{19}\text{F}$  MRI and  $^{89}\text{Zr}$  PET scans displayed colocalized hotspots in the inflamed right paw and minimal signal in the contralateral paw. Quantification of both  $^{19}\text{F}$  and  $^{89}\text{Zr}$  hotspots displayed more than 10-fold higher signal in the right paw than in the contralateral paw (Fig. 2C).

To evaluate in vivo PET detection at clinically relevant activity doses, we performed descending dose tests (3,700 to 37 kBq) for the injected FERM nanoemulsion in the acute inflammation model

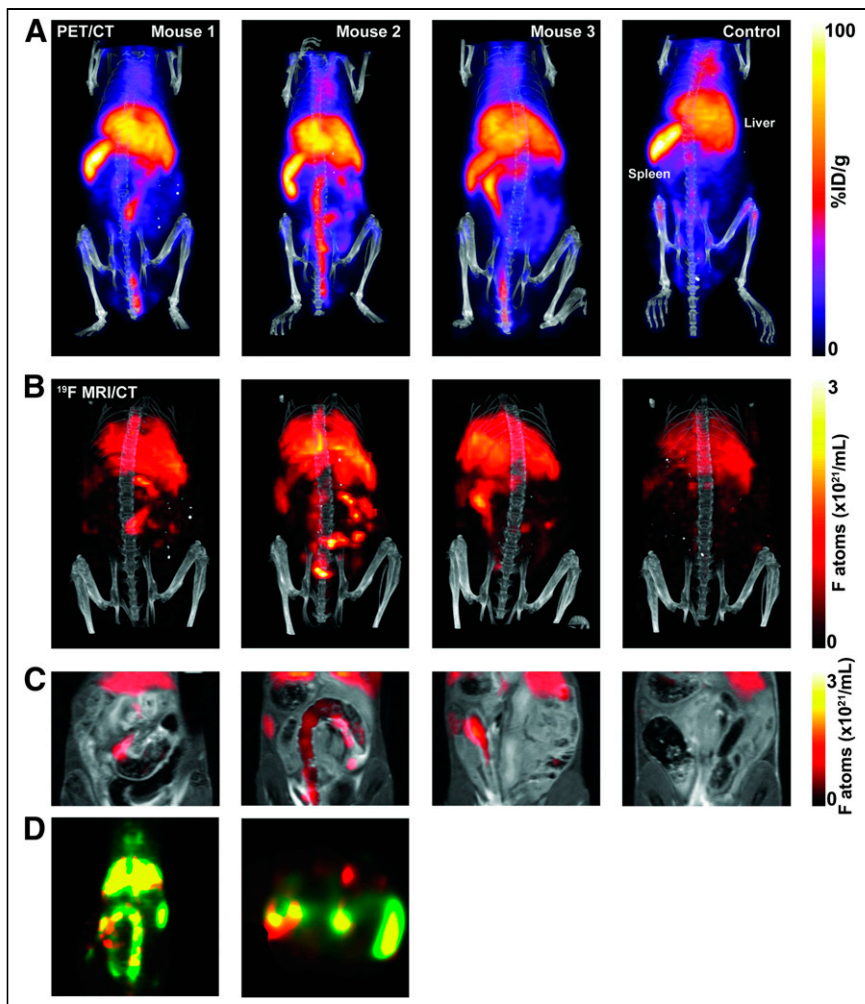


**FIGURE 3.** Multimodal PET and  $^{19}\text{F}$  MRI in IBD mice. (A) PET/CT images of 3 IBD mice and control (naïve) mice 24 h after intravenous injection of FERM nanoemulsion (3.7 MBq). (B) Composite  $^{19}\text{F}$  MRI/CT images of mice in A. (C) Overlaid  $^{19}\text{F}$  MRI and  $^1\text{H}$  MRI slices of mouse in B. (D) Composite PET and  $^{19}\text{F}$  MRI slices of coronal (left) and transverse (right) views.  $^{19}\text{F}$  MRI = red; PET = green; overlap = yellow.

(Fig. 2D). In clinical trials using  $^{89}\text{Zr}$  immuno-PET imaging, acceptable patient injection doses range from approximately 37 to 203.5 MBq, equivalent to 0.74–3.33 kBq per gram of body weight (assuming 60 kg/human) (17). For mice (~30 g), the corresponding clinical equivalent doses range from approximately 18.5 to 103.6 kBq. At all doses used, the ratio of uptake values in the right (inflamed) versus left (normal) paw was maintained at approximately 10 with statistical significance ( $P < 0.05$ ,  $n = 3$ ; Fig. 2D). At the lower doses, the inflammation foci remained the dominant image hotspot, thus showing inflammation specificity. At the 37-kBq level, the inflammation site remained clearly visible with a 10-min PET scan time. This translates to a human dose of 4 mL of FERM (18.5 MBq/mL), comprising about 0.8 g of fluorocarbon, a level that is an order of magnitude lower than historical artificial-blood-substitute doses (16). Overall, at clinically relevant activity doses, the inflammation diagnostic potential of FERM nanoemulsion appears to be maintained.

#### Visualization of IBD

Next, we explored the use of FERM for imaging IBD in a mouse model using PET and  $^{19}\text{F}$  MRI. The IBD model was induced by

adding dextran sulfate sodium salt to drinking water for C57BL/6 mice, resulting in ulcerative colitis-like inflammation with prominent inflammatory infiltrates, including macrophages in the gastrointestinal tract (29). IBD clinical symptoms peaked at approximately 8 d after the start of dextran sulfate sodium salt treatment. At peak, a single intravenous injection of  $^{89}\text{Zr}$ -FERM nanoemulsion ( $n = 5$ , 0.2 mL, 3.7 MBq,  $\sim 6 \times 10^{20}$  fluorine atoms) was administered, and 24 h thereafter  $^{89}\text{Zr}$  PET/CT and  $^{19}\text{F}/^1\text{H}$  MRI data were acquired. Representative images are shown in Figure 3, where both the PET and the  $^{19}\text{F}$  MRI data are coregistered to CT. Major hotspots were observed in the colon in  $^{89}\text{Zr}$  PET images for all IBD mice. IBD lesions are patchy and heterogenous among subjects (30) and are distributed in the ascending and descending colon. Control mice, without dextran sulfate sodium salt induction, displayed prominent uptake in the liver and spleen and minimal colon signal, as expected for RES clearance of FERM nanoemulsion.  $^{19}\text{F}$  MRI in the same animals also displayed inflammatory hotspots in the colon (Fig. 3B). Generally,  $^{19}\text{F}$  MRI lesion signals were more punctate than the relatively diffuse PET signals. Overlays of  $^{19}\text{F}$  and high-resolution  $^1\text{H}$  anatomic images showed  $^{19}\text{F}$  signal localization in the anatomic context of the colon wall (Fig. 3C). To quantitate inflammation in the bowel, ROIs were placed around the peritonea, and the resulting signal histograms for PET and  $^{19}\text{F}$  MRI were calculated (Supplemental Fig. 7). Both methods clearly showed a much larger proportion of high-signal voxels in the IBD

mice than in controls. Notably, the anatomic signal patterns for PET and  $^{19}\text{F}$  MRI were largely overlapping (Fig. 3D).

#### Visualization of Tumor-Associated Macrophages

Tumor-associated macrophages play a central role in the initiation, progression, and metastasis of tumors, and their density in the tumor microenvironment is often associated with tumor aggressiveness and patient survival rate (31). Imaging of tumor-associated macrophages and metastasis-associated macrophages may enable early detection of malignancy, as well as assessment of response to immunotherapies. We investigated the use of the FERM nanoemulsion for PET and  $^{19}\text{F}$  MRI macrophage imaging in a breast cancer mouse model (Fig. 4). Tumor cells (4T1) expressing luciferase were implanted in the mammary fat pad, and bioluminescence imaging confirmed primary tumor growth in the flank. FERM nanoemulsion PET and  $^{19}\text{F}$  MRI scans were conducted at 2 wk (early,  $n = 5$ ) or 5 wk (late,  $n = 5$ ) after implantation in separate cohorts. At 24 h before imaging, the animals received the  $^{89}\text{Zr}$ -FERM nanoemulsion intravenously (3.7 MBq,  $\sim 6 \times 10^{20}$  fluorine atoms). In the early

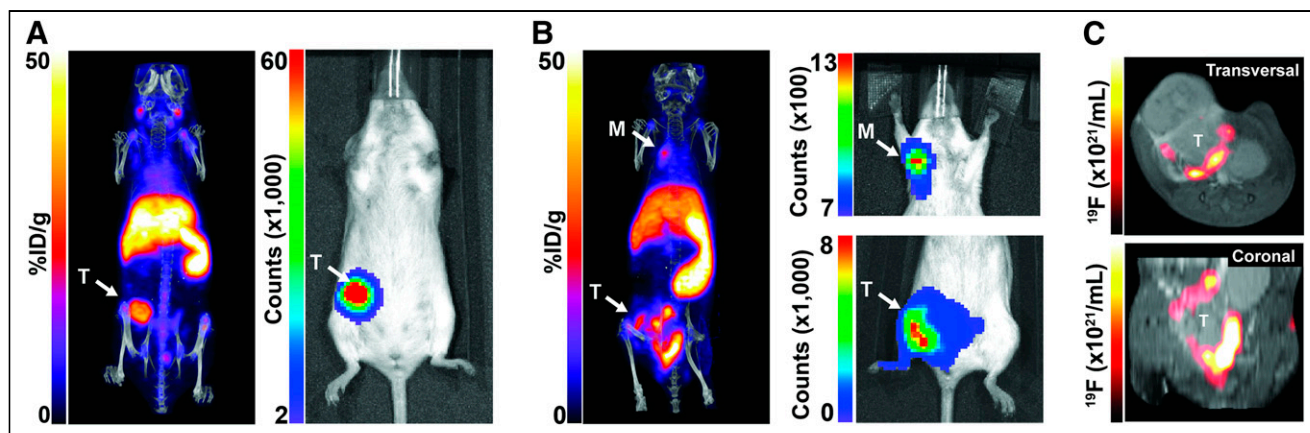


**FIGURE 4.** In vivo detection of tumor-associated macrophages and metastasis in 4T1 tumors using FERM nanoemulsion. (A and B) Representative PET/CT (left) and bioluminescence images (right) of mice 2 wk (A) and 5 wk (B) after implantation with 4T1 breast cancer cells. Bioluminescence images of metastasis in 5-wk group were acquired after shielding of primary tumor. (C) Overlaid  $^{19}\text{F}/^1\text{H}$  MRI slices at tumor site from same mouse as B, showing hotspots in tumor periphery consistent with tumor-associated macrophage localization. Metastasis is outside image field of view. T = tumor; M = metastasis.

cohort, PET images (Fig. 4A) displayed major hotspots in the whole tumor area, as well as in the liver and spleen. In the late group, FERM had a significant presence in the flank-tumor periphery for both PET and  $^{19}\text{F}$  MRI (Figs. 4B and 4C), with minimal signal in the tumor center, consistent with peripheral macrophage infiltration and tumor-core necrosis.  $\gamma$ -counting of the excised tumors confirmed high tumor uptake of the agent, with  $5.3 \pm 1.8$  %ID in early tumors and  $10.7 \pm 3.6$  %ID in late tumors. Notably, putative metastases were observed in the axillary lymph node region, visible with both PET and bioluminescence imaging (Fig. 4B), in 2 of 5 animals in the late cohort. In the late-cohort lungs, we observed slightly elevated, diffuse PET signal ( $n = 5$ ), which was not apparent on  $^{19}\text{F}$  MRI or bioluminescence imaging.

## DISCUSSION

In this article, we have described the development of an  $^{89}\text{Zr}$ -FERM nanoemulsion for imaging inflammatory disease with high specificity, sensitivity, and versatility, using both PET and  $^{19}\text{F}$  MRI. We devised a fluorine  $^{89}\text{Zr}$  chelator, FHOA, that effectively encapsulates the radioisotope into the nanoemulsion core. This strategy minimizes radioisotope leakage and nonspecific cell labeling. FHOA was prepared and purified at gram scale in a single run. FERM was formulated as a cold nanoemulsion preloaded with chelate and displayed long-term stability ( $>2$  mo). Before intravenous delivery, FERM was radiolabeled with  $^{89}\text{Zr}$  via simple premix and filtration steps. The use of  $^{89}\text{Zr}$ , with its relatively long half-life (3.3 d), allows for RES cell (macrophage) uptake of the nanoemulsion, as well as longitudinal studies over several days with a single administration.

The in vivo stability of the FERM nanoemulsion was evaluated by blood pharmacokinetic analysis, which suggested minimal dissociation in vivo. Both dosimetry and  $^{19}\text{F}$  NMR intensity analyses of serial blood samples displayed biexponential decreases over time; the slow time constant ( $\sim 15$  h), presumed to be RES uptake, indicates overall good agreement between the 2 measurement methods ( $>0.99$  correlation). Thus, the  $^{89}\text{Zr}$  and  $^{19}\text{F}$  signal generators stay cocomplexed during the RES uptake period. The fast-phase time constant, representing the initial blood perfusion of

the agent, varied when measured by dosimetry (half-time, 36 min) and  $^{19}\text{F}$  (half-time, 54 min;  $P < 0.05$ ). Variations in the timing of blood-sample  $\gamma$ -counting ( $\sim 1$ –4 min), imperfections in the gel-filtration purification, and the presence of residual  $^{89}\text{Zr}$  bound to lipid headgroups (32) of the surfactant all could potentially lead to measurement discrepancies in the fast-phase time constant.

Prior preclinical studies have used  $^{19}\text{F}$  MRI with fluorocarbons for macrophage labeling in situ, such as in myocarditis (9), solid-organ transplant rejection (33), IBD (27,34), and various cancer models (35–37). Importantly, these same studies firmly established intracellular tissue macrophage uptake of the fluorocarbon agent as the dominant image signal observed in vivo. For example, IBD studies have shown exclusive colocalization of a fluorescently conjugated fluorocarbon nanoemulsion and F4/80-positive macrophages in immunohistochemistry micrographs, as well as a correlation between the histopathology quantification of lesion burden in the colon wall and the total  $^{19}\text{F}$  signal in the same specimens (34). Additionally, quantitative PCR analysis correlating macrophage burden via CD68 RNA levels with  $^{19}\text{F}$  signal in colon samples has shown a linear relationship (27). Moreover, clodronate liposome treatment ablates the  $^{19}\text{F}$  signal in the colon of IBD mice (27). In solid-tumor models, immunohistochemistry has shown specific uptake of a fluorescent fluorocarbon nanoemulsion in macrophages both at the primary tumor periphery in late stages and at metastasis sites (35–38). Although fluorocarbon nanoemulsions have been widely studied for  $^{19}\text{F}$  MRI, descriptions of their use as a PET tracer have been very limited (39,40).

The FERM nanoemulsion shows promise for precise detection of a broad range of inflammatory lesions with high macrophage specificity. In the case of IBD, macrophages derived from blood monocytes are important mediators of chronic inflammation, along with T-helper types 1 and 2 T cells (41,42). The gold-standard IBD test is colonoscopic biopsy, an invasive procedure requiring multiple tissue bites for diagnosis, which may result in sampling errors and cause patient discomfort, thus driving the need for more precise diagnostics for staging and treatment-course monitoring. Physiologic bowel uptake of  $^{18}\text{F}$ -FDG is highly variable in the colon and can be quite intense, especially in patients taking metformin (43), thus limiting the usefulness of  $^{18}\text{F}$ -FDG. Oncology also presents another major area of use for

FERM for precision macrophage imaging, because of the diagnostic potential and the increasing focus on macrophages as therapeutic targets (44).

In both PET and  $^{19}\text{F}$  MRI, lesion foci are the only major hotspots other than the liver and spleen. Hotspots display anatomic similarities across both modalities, indicative of FERM stability in vivo. The MRI-apparent lesions appear more punctate than PET-detected lesions, which are more diffuse. There are fundamental differences between the 2 imaging techniques with regard to intrinsic sensitivity and resolution, image reconstruction methods, point-spread functions, and partial-volume effects that impact quantification and small-lesion appearance (45,46). A more concrete understanding of the interplay among these factors could be achieved by mathematic modeling in future studies. Generally,  $^{19}\text{F}$  MRI is prone to false-negative signals due to sensitivity limitations, whereas high-sensitivity PET imaging is prone to false-positives; thus, a bimodal readout could potentially provide a complementary representation of the ground-truth lesion macrophage distribution using a FERM nanoemulsion. As a practical matter,  $^{19}\text{F}$  is advantageous as a stable tag to assay nanoemulsion biodistribution via  $^{19}\text{F}$  NMR of tissue samples (47), as well as to assay the fate of the  $^{89}\text{Zr}$ -fluorocarbon complex when combined with  $\gamma$ -counting (e.g., Fig. 1C).

Although we acquired PET and  $^{19}\text{F}$  MRI using separate instruments, future advancements in imaging hardware may enable simultaneous acquisition of PET and  $^{19}\text{F}$  MRI data. Recently, dual-mode PET and  $^1\text{H}$ -only MRI scanners have been introduced to clinical service, such as for cardiology, oncology, and neurology (48). Whole-body clinical PET to identify putative lesions, followed by inflammation hotspot  $^{19}\text{F}/^1\text{H}$  MRI in a smaller field of view with high soft-tissue resolution, may yield a rich dataset for treatment planning and response monitoring.

Although the safety and detectability assessments for the FERM nanoemulsion are preliminary, the results suggest translational potential for a broad range of inflammatory disease types. One of the challenges with  $^{19}\text{F}$  MRI is that capabilities for X-nuclei imaging (e.g.,  $^{19}\text{F}$ ,  $^3\text{He}$ ,  $^{129}\text{Xe}$ ) are uncommon in a clinical setting compared with PET; thus, initial use will likely involve PET-only readouts. The scalable production of the FERM nanoemulsion, together with streamlined radiolabeling, may enable practical implementation in a clinical setting.

## CONCLUSION

The FERM nanoemulsion was shown to be effective for imaging of macrophage-associated inflammatory disease using PET and  $^{19}\text{F}$  MRI and was versatile in a range of preclinical models. The novel fluorine  $^{89}\text{Zr}$  chelator FHOA encapsulates the radioisotope into the nanoemulsion core, which minimizes radioisotope leakage and nonspecific cell labeling. The FERM nanoemulsion may open new avenues for precise stratification, diagnosis, and treatment monitoring in cases in which normal physiologic uptake of  $^{18}\text{F}$ -FDG may obscure the cellular inflammatory component of disease.

## DISCLOSURE

This research was supported by the National Institutes of Health (grants R01-EB024015 and R01-CA134633) and the California Institute for Regenerative Medicine (grant LA1-C12-06919). Eric Ahrens is a founder and shareholder of Celsense, Inc. No

other potential conflict of interest relevant to this article was reported.

## KEY POINTS

**QUESTION:** Can we use FERM for multimodal PET and  $^{19}\text{F}$  MRI of inflammatory macrophages?

**PERTINENT FINDINGS:** FERM was readily complexed before use and stable in vivo. Intravenous injection enabled multimodal imaging of inflammatory hotspots with high specificity in acute inflammation, IBD, and solid-tumor rodent models.

**IMPLICATIONS FOR PATIENT CARE:** The  $^{89}\text{Zr}$  nanoemulsion technology may provide a new approach to precise stratification, diagnosis, and treatment monitoring in a range of inflammatory diseases.

## REFERENCES

1. Hammoud DA. Molecular imaging of inflammation: current status. *J Nucl Med*. 2016;57:1161–1165.
2. Rosenbaum SJ, Lind T, Antoch G, Bockisch A. False-positive FDG PET uptake: the role of PET/CT. *Eur Radiol*. 2006;16:1054–1065.
3. Hamidzadeh R, Eftekhari A, Wiley EA, Wilson D, Alden T, Bénard F. Metformin discontinuation prior to FDG PET/CT: a randomized controlled study to compare 24- and 48-hour bowel activity. *Radiology*. 2018;289:418–425.
4. Tahara N, Mukherjee J, de Haas HJ, et al. 2-deoxy-2-[ $^{18}\text{F}$ ]fluoro-D-mannose positron emission tomography imaging in atherosclerosis. *Nat Med*. 2014;20:215–219.
5. Wu C, Li F, Niu G, Chen X. PET imaging of inflammation biomarkers. *Theranostics*. 2013;3:448–466.
6. Keliher EJ, Ye YX, Wojtkiewicz GR, et al. Polyglucose nanoparticles with renal elimination and macrophage avidity facilitate PET imaging in ischaemic heart disease. *Nat Commun*. 2017;8:14064–14076.
7. Kim HY, Li R, Ng TSC, et al. Quantitative imaging of tumor-associated macrophages and their response to therapy using  $^{64}\text{Cu}$ -labeled Macrin. *ACS Nano*. 2018;12:12015–12029.
8. Keliher EJ, Yoo J, Nahrendorf M, et al.  $^{89}\text{Zr}$ -labeled dextran nanoparticles allow in vivo macrophage imaging. *Bioconjug Chem*. 2011;22:2383–2389.
9. Flögel U, Ding Z, Hardung H, et al. In vivo monitoring of inflammation after cardiac and cerebral ischemia by fluorine magnetic resonance imaging. *Circulation*. 2008;118:140–148.
10. Temme S, Bonner F, Schrader J, Flögel U.  $^{19}\text{F}$  magnetic resonance imaging of endogenous macrophages in inflammation. *Wiley Interdiscip Rev Nanomed Nanobiotechnol*. 2012;4:329–343.
11. Ahrens ET, Flores R, Xu H, Morel PA. In vivo imaging platform for tracking immunotherapeutic cells. *Nat Biotechnol*. 2005;23:983–987.
12. Isaacs RE, Bender AS, Kim CY, Shi YF, Norenberg MD. Effect of osmolality and anion channel inhibitors on myo-inositol efflux in cultured astrocytes. *J Neurosci Res*. 1999;57:866–871.
13. Fairclough M, Prenant C, Ellis B, et al. A new technique for the radiolabelling of mixed leukocytes with zirconium-89 for inflammation imaging with positron emission tomography. *J Labelled Comp Radiopharm*. 2016;59:270–276.
14. Squires JE. Artificial blood. *Science*. 2002;295:1002–1005.
15. Ahrens ET, Helfer BM, O'Hanlon CF, Schirra C. Clinical cell therapy imaging using a perfluorocarbon tracer and fluorine-19 MRI. *Magn Reson Med*. 2014;72:1696–1701.
16. Riess JG. Understanding the fundamentals of perfluorocarbons and perfluorocarbon emulsions relevant to in vivo oxygen delivery. *Artif Cells Blood Substit Immobil Biotechnol*. 2005;33:47–63.
17. Jauw YW, Menke-van der Houven van Oordt CW, Hoekstra OS, et al. Immuno-positron emission tomography with zirconium-89-labeled monoclonal antibodies in oncology: what can we learn from initial clinical trials? *Front Pharmacol*. 2016;7:131.
18. Koshti N, Reddy GV, Jacobs H, Gopalan A. Convenient synthetic methods for the preparation of N-fluoroalkylhydroxamic acids. *Synth Commun*. 2002;32:3779–3790.
19. Deri MA, Zeglis BM, Francesconi LC, Lewis JS. PET imaging with  $^{89}\text{Zr}$ : from radiochemistry to the clinic. *Nucl Med Biol*. 2013;40:3–14.



20. Patra M, Bauman A, Mari C, et al. An octadentate bifunctional chelating agent for the development of stable zirconium-89 based molecular imaging probes. *Chem Commun (Camb)*. 2014;50:11523–11525.
21. Guérard F, Lee YS, Tripier R, Szajek LP, Deschamps JR, Brechbiel MW. Investigation of Zr(IV) and <sup>89</sup>Zr(IV) complexation with hydroxamates: progress towards designing a better chelator than desferrioxamine B for immuno-PET imaging. *Chem Commun (Camb)*. 2013;49:1002–1004.
22. Rothe M, Jahn A, Weiss K, et al. In vivo <sup>19</sup>F MR inflammation imaging after myocardial infarction in a large animal model at 3T. *MAGMA*. 2019;32:5–13.
23. Kislukhin AA, Xu H, Adams SR, Narsinh KH, Tsiens RY, Ahrens ET. Paramagnetic fluorinated nanoemulsions for sensitive cellular fluorine-19 magnetic resonance imaging. *Nat Mater*. 2016;15:662–668.
24. Efron B, Tibshirani RJ. An Introduction to the Bootstrap. Chapman and Hall/CRC Press; 1994:4.
25. Neubauer AM, Sim H, Winter PM, et al. Nanoparticle pharmacokinetic profiling in vivo using magnetic resonance imaging. *Magn Reson Med*. 2008;60:1353–1361.
26. Posadas I, Bucci M, Roviezzo F, et al. Carrageenan-induced mouse paw oedema is biphasic, age-weight dependent and displays differential nitric oxide cyclooxygenase-2 expression. *Br J Pharmacol*. 2004;142:331–338.
27. Kadayakkara DK, Ranganathan S, Young WB, Ahrens ET. Assaying macrophage activity in a murine model of inflammatory bowel disease using fluorine-19 MRI. *Lab Invest*. 2012;92:636–645.
28. Abou DS, Ku T, Smith-Jones PM. In vivo biodistribution and accumulation of <sup>89</sup>Zr in mice. *Nucl Med Biol*. 2011;38:675–681.
29. Na YR, Stakenborg M, Seok SH, Matteoli G. Macrophages in intestinal inflammation and resolution: a potential therapeutic target in IBD. *Nat Rev Gastroenterol Hepatol*. 2019;16:531–543.
30. Cho JH, Feldman M. Heterogeneity of autoimmune diseases: pathophysiologic insights from genetics and implications for new therapies. *Nat Med*. 2015;21:730–738.
31. Qian BZ, Pollard JW. Macrophage diversity enhances tumor progression and metastasis. *Cell*. 2010;141:39–51.
32. Abou DS, Thorek DL, Ramos NN, et al. <sup>89</sup>Zr-labeled paramagnetic octreotide-liposomes for PET-MR imaging of cancer. *Pharm Res*. 2013;30:878–888.
33. Hitchens TK, Ye Q, Eytan DF, Janjic JM, Ahrens ET, Ho C. F-19 MRI detection of acute allograft rejection with in vivo perfluorocarbon labeling of immune cells. *Magn Reson Med*. 2011;65:1144–1153.
34. Shin SH, Kadayakkara DK, Bulte JW. In vivo <sup>19</sup>F MR imaging cell tracking of inflammatory macrophages and site-specific development of colitis-associated dysplasia. *Radiology*. 2017;282:194–201.
35. Khurana A, Chapelin F, Xu H, et al. Visualization of macrophage recruitment in head and neck carcinoma model using fluorine-19 magnetic resonance imaging. *Magn Reson Med*. 2018;79:1972–1980.
36. Makela AV, Gaudet JM, Foster PJ. Quantifying tumor associated macrophages in breast cancer: a comparison of iron and fluorine-based MRI cell tracking. *Sci Rep*. 2017;7:42109.
37. Makela AV, Foster PJ. Imaging macrophage distribution and density in mammary tumors and lung metastases using fluorine-19 MRI cell tracking. *Magn Reson Med*. 2018;80:1138–1147.
38. Balducci A, Wen Y, Zhang Y, et al. A novel probe for the non-invasive detection of tumor-associated inflammation. *Oncol Immunology*. 2013;2:e23034.
39. Fabiilli ML, Piert MR, Koeppe RA, Sherman PS, Quesada CA, Kripfgans OD. Assessment of the biodistribution of an [<sup>18</sup>F]FDG-loaded perfluorocarbon double emulsion using dynamic micro-PET in rats. *Contrast Media Mol Imaging*. 2013;8:366–374.
40. Amir N, Green D, Kent J, et al. <sup>18</sup>F-labeled perfluorocarbon droplets for positron emission tomography imaging. *Nucl Med Biol*. 2017;54:27–33.
41. Sheikh SZ, Plevy SE. The role of the macrophage in sentinel responses in intestinal immunity. *Curr Opin Gastroenterol*. 2010;26:578–582.
42. Mahida YR. The key role of macrophages in the immunopathogenesis of inflammatory bowel disease. *Inflamm Bowel Dis*. 2000;6:21–33.
43. Gontier E, Fourme E, Wartski M, et al. High and typical <sup>18</sup>F-FDG bowel uptake in patients treated with metformin. *Eur J Nucl Med Mol Imaging*. 2008;35:95–99.
44. Mantovani A, Marchesi F, Malesci A, Laghi L, Allavena P. Tumour-associated macrophages as treatment targets in oncology. *Nat Rev Clin Oncol*. 2017;14:399–416.
45. Rahmim A, Qi J, Sossi V. Resolution modeling in PET imaging: theory, practice, benefits, and pitfalls. *Med Phys*. 2013;40:064301.
46. Robson MD, Gore JC, Constable RT. Measurement of the point spread function in MRI using constant time imaging. *Magn Reson Med*. 1997;38:733–740.
47. Ahrens ET, Young W-B, Xu H, Pusateri LK. Rapid quantification of inflammation in tissue samples using perfluorocarbon emulsion and fluorine-19 nuclear magnetic resonance. *Biotechniques*. 2011;50:229–234.
48. Broski SM, Goenka AH, Kemp BJ, Johnson GB. Clinical PET/MRI: 2018 update. *AJR*. 2018;211:295–313.